

Quorum sensing of light-activated colloids in nematic liquid crystals

Antonio Tavera-Vázquez^{1*}, David Martin^{2,3}, Haijie Ren⁴, Sam Rubin¹,
Andrés Córdoba^{1,5}, Rui Zhang⁴, Vincenzo Vitelli^{2,6}, Juan J. de Pablo^{1,7,8,9*}

^{1*}Pritzker School of Molecular Engineering, University of Chicago, Chicago, 60637, IL, USA.

²Leinweber Institute for Theoretical Physics, University of Chicago, Chicago, 60637, IL, USA.

³LPTMC, Sorbonne Université & CNRS, Paris, 75252, France.

⁴Department of Physics, Hong Kong University of Science and Technology, Hong Kong, 10587,
Hong Kong, China.

⁵Área de Ciencias Fundamentales, Escuela de Ciencias Aplicadas e Ingeniería, Universidad
EAFIT, Medellín, 050022, Colombia.

⁶James Franck Institute, University of Chicago, Chicago, 60637, IL, USA.

^{7*}Chemical and Biomolecular Engineering, Tandon School of Engineering, New York University,
Brooklyn, 11201, NY, USA.

^{8*}Courant Institute of Mathematical Sciences, New York University, Manhattan, 10012, NY, USA.

^{9*}Department of Physics, New York University, Brooklyn, 11201, NY, USA.

*Corresponding author(s). E-mail(s): atv.tavera@gmail.com ; jjd8110@nyu.edu ;

Abstract

Motile living organisms routinely probe their surroundings to adapt in ever-evolving environments. Although synthetic microswimmers offer surrogates for self-propelled living entities, they often lack the complex feedback mechanisms that enable organisms to adapt. In this work, we present an experimental platform in which light-activated colloids dispersed in a nematic liquid crystal can (i) switch from directed to active Brownian motion depending on the nematic anchoring and (ii) mechanically adjust their motility in response to crowding, effectively enforcing quorum-sensing interactions. Both features are caused by a distinctive self-propulsion mechanism as unveiled through experiments, simulations, and theory. We characterize the dynamics of a single colloid and demonstrate that its motion is captured by an active Brownian particle model if the nematic anchoring is homeotropic, and by directed self-propulsion along the nematic director if the anchoring is planar. Next, we investigate the many-body dynamics, showing that it undergoes a clustering phase separation through effective quorum-sensing interactions. Our work suggests how to create adaptive materials with life-like capabilities using readily accessible properties of liquid crystals and colloids without explicitly engineering any of the needed mechano-chemical feedbacks.

Keywords: Liquid crystals, Active matter, Microswimmers, Phase transitions, Light-activation

The survival of living organisms depends on their ability to sense their surroundings and react adaptively: bacteria perform chemotaxis to forage food

sources [1, 2], plant growth is regulated by neighboring foliage density [3], and birds adapt their flight to remain in the flock [4]. A minimal model for such

self-regulation is quorum sensing, where entities modify their dynamics in response to interactions with their neighbors [5, 6]. Although synthetic active particles have proved a controlled testbed for studying the collective behavior of living entities, they are typically made of inanimate beads that lack the ability to perform quorum-sensing interactions [7–12]. Until now, the study of self-regulation mechanisms and their corresponding many-body emergent behavior has focused on computer-controlled active units [13–16] or dense assemblies of Quincke rollers [17] and rods [18].

In this paper, we report how Janus particles evolving in a nematic liquid crystal (LC) spontaneously self-propel and perform quorum-sensing by light activation. We show how the structured anisotropic LC enables control over the dynamics of the colloids, directing them in a specific direction and endowing them with additional activity regulation through quorum-sensing. Our efforts are fourfold. First, we describe the experimental setup, detailing the interplay between the mesogens and the Janus particles, be it in the presence or in the absence of light. We further validate our experimental observations with continuum numerical simulations of the LC. Second, we characterize the non-equilibrium mechanism behind the emergence of self-propulsion through a qualitative derivation further supported by numerical simulations. Third, we probe the dynamics of a single Janus colloid and propose corresponding phenomenological models inspired by active matter. Lastly, we explore the many-body dynamics, showing that colloids perform an effective quorum-sensing slow down, which ultimately leads to the emergence of a clustered phase.

Experimental setup

Our platform consists of a rectangular cell with dimensions 2×2 cm and height of $12 \mu\text{m}$ filled with a suspension of silica spheres $10 \mu\text{m}$, half coated with a light absorbent titanium layer. A single LED source that shines from above throughout the cell controls the light intensity (see Fig. 1). Upon illuminating a Janus colloid, its metal layer heats up the surrounding LC and induces a local nematic to isotropic transition, resulting in the formation of a disordered LC bubble attached to the coated side. Such a configuration frustrates the orientation of the mesogens at the contact line between the bubble and the colloid because the anchoring is homeotropic on silica but approximately planar on the bubble’s surface. Hence, nematic defects

emerge in order to ensure the continuity of the director field near the contact line. As detailed in the next section, the presence of these defects leads to a net self-propulsion force which, depending on the experimental conditions, we found to be either parallel or antiparallel to the bead’s revolution axis (see Fig. 1d and i).

We studied two different treatments of the cell surface resulting in homeotropic and planar anchoring of the mesogens (details for their experimental manufacturing can be found in the Methods). As shown in Fig. 1, these two distinct orientations at the boundary deeply impact the configuration of the defects around the colloid, since the continuity of the director field must be preserved everywhere. Consequently, the defect structures are affected by the anchoring and so is the resulting dynamics of the colloid. In the remainder of this paper, we will thus distinguish between these two scenarios, namely homeotropic and planar anchoring, and we will specify our results for each of these two cases.

Homeotropic confinement, as shown on the left side of Fig. 1, induces a nematic order along the z direction far from the colloid (see Fig. 1a). Close to the bead, the LC’s configuration is light-dependent: the passive, non-illuminated case is displayed in the upper row of Fig. 1 while the active, illuminated case is shown in the lower row.

Passive: Cross-polarized microscopy (Fig. 1c) exhibits a birefringence pattern with four bright lobes, thus confirming the homeotropic anchoring of the mesogens on the surface of the bead. The frustration between the bulk’s mesogens and the director field close to the colloid generates a Saturn ring defect located in the bead’s equatorial plane, parallel to the cell’s surfaces (see orange line in Fig. 1a) [19].

Active: The light-generated bubble of isotropic LC breaks the rotational symmetry of the nematic field around z (see the Fig. 1d sketch). As shown in Fig. 1e, cross-polarized microscopy only reports two birefringence lobes located on the bare or non-coated hemisphere, confirming an anchoring change of the mesogens on the bubble’s surface. This generates two additional regions of geometric frustration for the director field that were absent in the passive case. The first one is located at the contact line between the bubble and the colloid, where planarly-anchored mesogens must encounter their homeotropically-anchored counterpart. This first source of frustration is relaxed by the formation of an off-centered Saturn ring at the contact line (yz plane), as shown in Fig. 1d. The

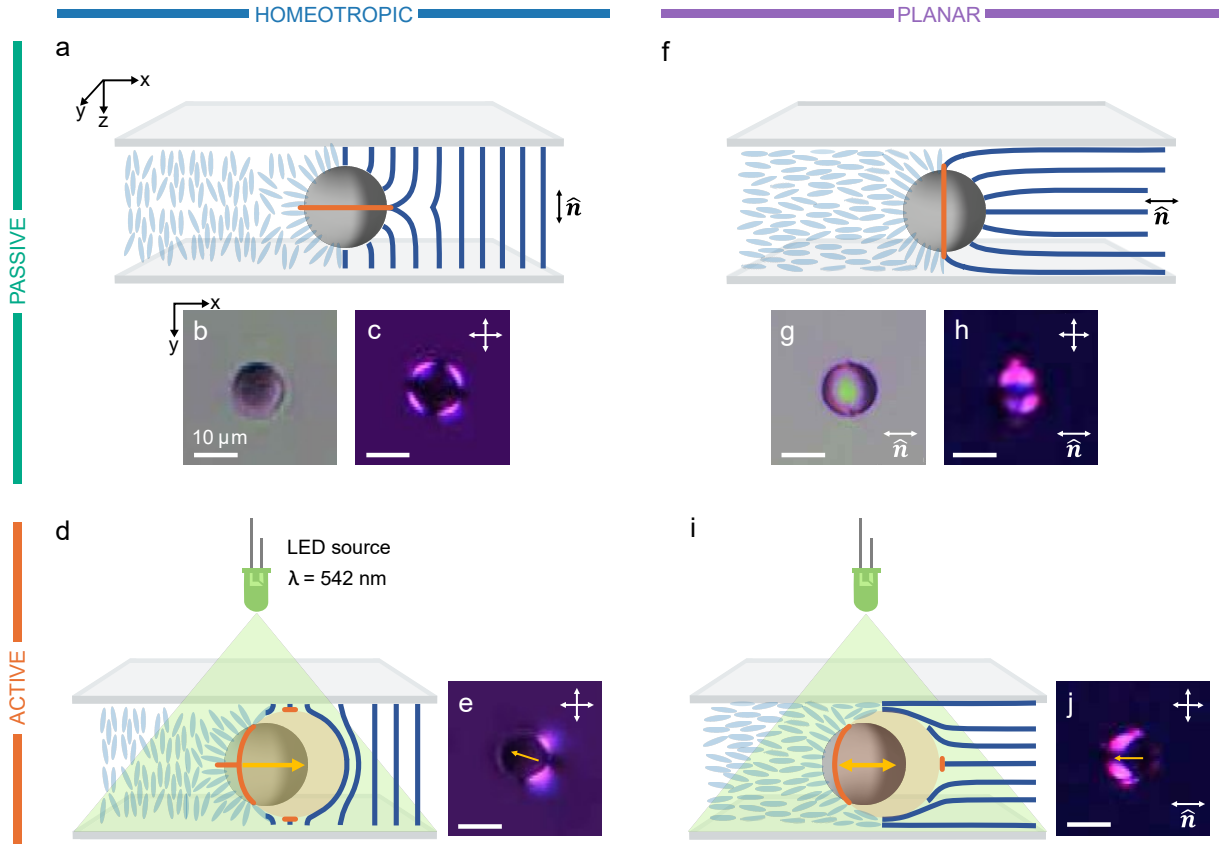


Figure 1: Visualization of the LC configuration around a Janus colloid with homeotropic (left) and planar (right) anchoring at the confining cell, as well as in the absence (top) or presence (bottom) of activation light. **a,f,d,i** Schematic view of the mesogens around the colloid. The darker area (right side) marks the coated side of the particle while the region thinly colored in orange indicates the bubble of the isotropic phase. The unit vector \hat{n} is the bulk's nematic director, blue lines represent the nematic field, while orange lines indicate topological defects. Finally, the yellow arrow indicates the potential directions of the emerging motility: in the planar case, the colloid can self-propel toward or away from the coated side. **b,g** Brightfield experimental snapshots of a Janus particle. **c,e,h,j** Cross-polarized experimental snapshots of a Janus particle. In **c**, the birefringent bright lobes are characteristic of a Saturn ring located in the xy plane. In **h,j**, small bumps at the particles' surface suggest the presence of Saturn rings in the yz plane. All scale bars represent $10 \mu\text{m}$.

second region of frustration is located at the top and bottom tips of the bubble, where mesogens strongly favor homeotropic anchoring at the cell's surface. This second source of frustration is relaxed by the formation of two boojum defects [20, 21], as shown in Fig. 1d. Note that the colloid always self-propels toward the coated hemisphere.

Planar anchoring, as shown on the right hand side of Fig. 1, induces a nematic order along the x direction in the bulk (see Fig. 1f). Similarly to homeotropic confinement, the behavior of the mesogens close to the

bead is light dependent.

Passive: In brightfield microscopy (see (Fig. 1g)), we observe two lumps located at the top and bottom of the colloid. These lumps are characteristic of a Saturn ring located in the yz plane (orange line in Fig. 1f) whose presence is further confirmed in cross-polarized microscopy (Fig. 1h). This defect ring stems from the frustration between the homeotropically anchored mesogens at the surface of the bead and their planar anchored counterparts at the cell's surface.

Active: The light-generated isotropic bubble forces

the reconfiguration of the mesogens (see Fig. 1i). Cross-polarized microscopy (Fig. 1j) exhibits the two characteristic lumps of a Saturn ring located at the contact line between the isotropic bubble and the colloid (see the orange line in Fig. 1i). A new source of frustration also emerges at the right tip of the bubble, since the bulk mesogens must continuously distort to match the planar anchoring at the nematic-isotropic (NI) interface. This second source of frustration is relaxed by the emergence of a Bojuum defect located at the right tip of the bubble, as shown in Fig. 1i. Note that the particle's motility always emerges parallel to the bulk nematic director (x axis), but can be directed toward or away from the coated hemisphere, depending on the light intensity.

To support these experimental observations, we further performed numerical simulations of the LC around the colloid-bubble compound. As shown in Fig. 2, our simulations reveal the nematic director field S_0 with its defect structure (Fig. 2a-c) as well as the force distribution (Fig. 2d-f) at the surface of the system. The details of our non-equilibrium numerical approach, which uses two different temperatures in the distinct LC's phases, can be found in the Methods. For both homeotropic and planar confinements, our simulations confirm the experimental configuration of the LC reported in Fig. 1 and predict the direction of the emerging self-propulsion force.

For homeotropic confinement, Fig. 2a shows the emergence of a vertical defect ring at the contact line between the particle and the isotropic bubble, following the continued ring in the horizontal equatorial plane of the bare hemisphere. In addition, simulations show two boojum defects located at the bubble's top and bottom tips. Finally, the net force applied to the particle always remains positive in the numerical calculations, i.e. $F_x > 0$: the colloid only self-propels toward its coated side (see Fig. 2d).

For planar confinement, Fig. 2b and c, respectively, show the nematic field with their defects' configuration at low and high activation light intensities. Independently of the illumination, a vertical Saturn ring is formed at the contact line between the isotropic bubble and the particle. In addition, simulations show the emergence of a boojum defect at the right tip of the bubble, confirming our experimental findings. At low light intensity, the bubble's covering on the particle is minimal and we found a self-propulsion directed toward the coated side ($F_x > 0$, see Fig. 2e). At higher light intensity, the bubble's covering further increases and we found a self-propulsion directed away from

the coated side ($F_x < 0$, see Fig. 2f) in this scenario.

Finally, simulations show that the magnitude $|F_x|$ of the self-propulsion force is higher with homeotropic confinement than with planar confinement; a discrepancy that is further confirmed experimentally. In the next section, we present a qualitative model describing the emergence of the colloid's motility. In particular, our model reveals how the bubble's covering (and therefore the light intensity) controls the direction of the motility in the case of planar confinement.

Self-propulsion mechanism

To characterize the self-propulsion mechanism, we analyze the force distribution on the surface of the particle-bubble system. The stress tensor σ exerted on the activated particle can be decomposed into three components as $\sigma = P_p \mathbf{1}_{S_p} \mathbb{1} + P_b \mathbf{1}_{S_b} \mathbb{1} + \sigma^{\text{defect}}$, where $\mathbf{1}$ and $\mathbb{1}$ are, respectively, the indicator function and the identity. The first contribution represents the pressure exerted on S_p , the surface of the particle uncovered by the bubble. The second contribution similarly represents the pressure exerted on S_b , the surface of the bubble. Finally, the third contribution σ^{defect} is an additional inhomogeneous stress tensor arising from the presence of topological defects (Saturn rings and boojums). Far from these defects, the force exerted on a surface $d\mathbf{S}$ of the system is therefore, respectively, $-P_p d\mathbf{S}$ on S_p and $-P_b d\mathbf{S}$ on S_b . We will further assume that the pressures P_p and P_b are constant and induced by splay deformations such that $P_p \propto K_1^p/R_p^2$ and $P_b \propto K_1^b/R_b^2$, with K_1^p , R_p and K_1^b , R_b being respectively the splay modulus and radius of the particle and bubble. Note that the splay modulus depends on the local director field, which decreases with temperature. Since the bubble remains at a higher temperature than the surrounding LC, we therefore have $K_1^b < K_1^p$. In addition, we experimentally observe that $R_b > R_p$, hence entailing $P_b < P_p$. The x component of the total force exerted on the system is obtained by projecting $\int \sigma \cdot d\mathbf{S}$ onto e_x and reads (see Methods)

$$F_x = F_x^P + F_x^{\text{defect}} = \pi h^2 \Delta P + F_x^{\text{defect}}, \quad (1)$$

where $\Delta P = (P_p - P_b) > 0$, h is the radius of the contact circle between the bubble and the bead, and F_x^{defect} is the x component of the defect-generated force $\int \sigma^{\text{defect}} \cdot d\mathbf{S}$ (see Fig. 5).

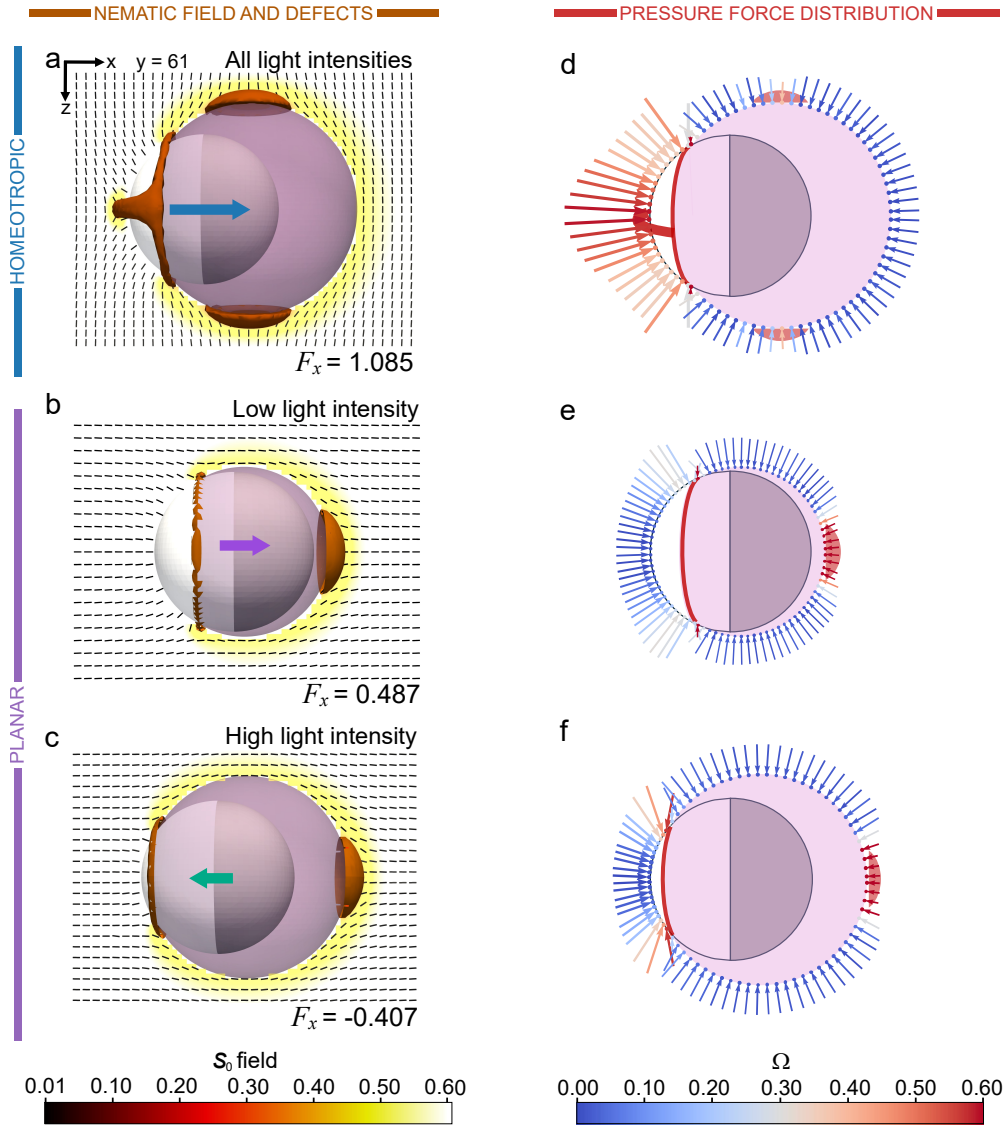


Figure 2: Continuum simulations of the colloid-isotropic bubble system for homeotropic (top) and planar (bottom) anchoring, showing the nematic field with its topological defects (left) as well as the pressure force distribution (right). **a,b,c** Topological defects are indicated by orange surfaces, the isotropic bubble is represented by the lightly opaque magenta color, located under the darker side of the colloid, which indicates its coated side. The colormap shows the magnitude of the scalar order parameter field S_0 , and the arrow indicates the direction of the net self-propulsion force F_x . In **a**, an off-centered Saturn ring is located at the contact line between the isotropic bubble and the colloid, as an extension of the Saturn ring that remains at the xy plane of the non-coated hemisphere. Two other localized topological point-like defects are further present at the bottom and at the top of the isotropic bubble. In **b,c**, an off-centered Saturn ring is located at the contact line between the isotropic bubble and the colloid. Another localized topological point-like defect is situated at the right tip of the isotropic bubble. As is noticed, increasing the light intensity leads to an increased covering of the colloid by the isotropic bubble. **d, e, f** Force distribution on the particle-bubble compound corresponding to panels **a, b**, and **c**. The colormap of the arrows, denoted as Ω , indicates the magnitude of the force's component due to the presence of defects, namely $\sigma^{\text{defect}} dS$. It is defined as $\Omega = \left| \frac{\mathbf{F}_{sim} \cdot \mathbf{P}_s}{|\mathbf{F}_{sim}|^2} - 1 \right|$, with \mathbf{F}_{sim} the numerically computed force while the pressure P_s can take two values: P_p on the particle surface or P_b on the bubble's surface. Thus, Ω deviates from zero only when the local defects contribute to the force. Further details on simulations are provided in the Methods.

For homeotropic confinement, the Saturn ring is located in the equatorial plane xy and remains localized on S_p . Therefore, it always pushes the colloid in the x direction and F_x^{defect} remains positive. Consequently, (1) indicates that the particle always self-propels toward the coated hemisphere, regardless of the light intensity.

For planar confinement, we use numerical simulations (see Methods) to show that

$$F_x^{\text{defect}} = -C \sin(2\theta_b), \quad (2)$$

where C is a positive constant and θ_b is the polar angle of the contact line between the bubble and the bead (see Figure 5 for a graphical definition of θ_b). Therefore, F_x^{defect} changes sign at $\theta_b = \pi/2$. When the illumination is weak, the bubble coverage is small, and $\theta_b > \pi/2$. In this case, F_x^{defect} remains positive and the colloid moves toward the coated hemisphere. When the illumination is intense, the bubble coverage is large, and $\theta_b < \pi/2$. In this case, F_x^{defect} becomes negative. If $\theta_b < \arctan(\frac{C}{\pi R_b^2 \Delta P})$, F_x^{defect} exceeds the pressure forces and the particle propels away from the coated hemisphere. Eq (1) hence also describes the reversal of motility observed experimentally upon varying the light intensity when the confinement is planar.

Single-body active dynamics

We now describe the colloid's trajectory under various light intensities expressed as a percentage value of a maximum irradiance of $257.50 \pm 0.50 \text{ mW mm}^{-2}$. We start our analysis with the case of homeotropic confinement, which corresponds to the left column of Fig. 3 (for a complete trajectory, see Fig. 3a) as well as to the supplementary movie Mov1. We conducted experiments at three irradiance values: $30.20 \pm 0.58 \%$, $34.51 \pm 0.66 \%$, and $43.14 \pm 0.83 \%$. As highlighted in Fig. 3b-d, both the bubble's radius and the colloid's self-propulsion increase with light intensity: as intuitively expected, symmetry breaking increases with illumination. The experimental mean-square displacements (MSDs) for the three irradiances are displayed in Fig. 3 e. They all feature an intermediate-time ballistic regime where $\langle r^2 \rangle \propto t^2$ and a long-time diffusive regime where $\langle r^2 \rangle \propto t$ (details on the tracking methodology and MSD's determination can be found in the Methods). Fig. 3f shows the steady-state speed as a function of light intensity: consistently with numerical simulations, it increases monotonically.

In the case of planar confinement, we carried out experiments at irradiances $20 \pm 0.23 \%$, $22.5 \pm 0.24 \%$, and $30 \pm 0.25 \%$. The results are summarized on the right side of Fig. 3. Typical trajectories of the colloids are displayed in Fig. 3g; the particles are restricted to move in the direction of the nematic director. However, they can either self-propel toward (negative speed) or away from (positive speed) the coated side depending on the light intensity, as shown in Fig. 3h-j and supplementary movies Mov2, Mov3 and Mov4. The illumination threshold of 22.5% marks the motility's reversal: at lower light intensities, v remains constant around $\sim -0.5 \mu\text{m s}^{-1}$, while for higher intensities it monotonically increases to reach values close to $1.5 \mu\text{m s}^{-1}$ (see Fig. 3l). MSDs are reported in Fig. 3k for various irradiances: they all feature a long-time ballistic regime where $\langle r^2 \rangle \propto t^2$.

We are now set up to devise a theoretical model that accounts for these features. The most prominent experimental signature that constrains modeling is the MSD. Leveraging active matter dynamics, we build two minimal models compatible with this signature for each type of confinement.

For homeotropic confinement, the direction of the self-propulsion of the particle remains unconstrained. We thus model the colloid as an Active Brownian Particle (ABP) [22, 23], assuming that its position $\mathbf{r}(t)$ and orientation $\phi(t)$ follow.

$$\dot{\mathbf{r}} = v\mathbf{u}(\phi) + \sqrt{2T}\boldsymbol{\eta}, \quad \dot{\phi} = \sqrt{2D}\xi, \quad (3)$$

where v is the speed magnitude, $\phi(\mathbf{u}(\phi))$ is the polar angle (unit vector) of the velocity direction in the xy plane, T and D controls the amplitude of translational and angular fluctuations, ξ is a Gaussian white noise of unit variance, and $\boldsymbol{\eta}$ is a Gaussian vector with independent components of unit variance. The MSD $\langle \Delta \mathbf{r}^2 \rangle$ of dynamics (3) has three distinct regimes; a diffusive one at small times, where $\langle \Delta \mathbf{r}^2 \rangle \sim 4Tt$, a ballistic regime at intermediate times where $\langle \Delta \mathbf{r}^2 \rangle \sim v^2 t^2$ and a diffusive regime at long times where $\langle \Delta \mathbf{r}^2 \rangle \sim 2\left(\frac{v^2}{D} + 2T\right)t$. Using these three regimes and our experimental determination of the MSD, we can therefore extract the values of v , T and D that best describe the colloid dynamics. We detail our fitting methodology in the Methods and report the corresponding results in Table 1. Finally, we simulated (3) and superimposed the resulting MSD on the experimental measurements in Fig. 3e, proving the validity of (3) with our fitted parameters.

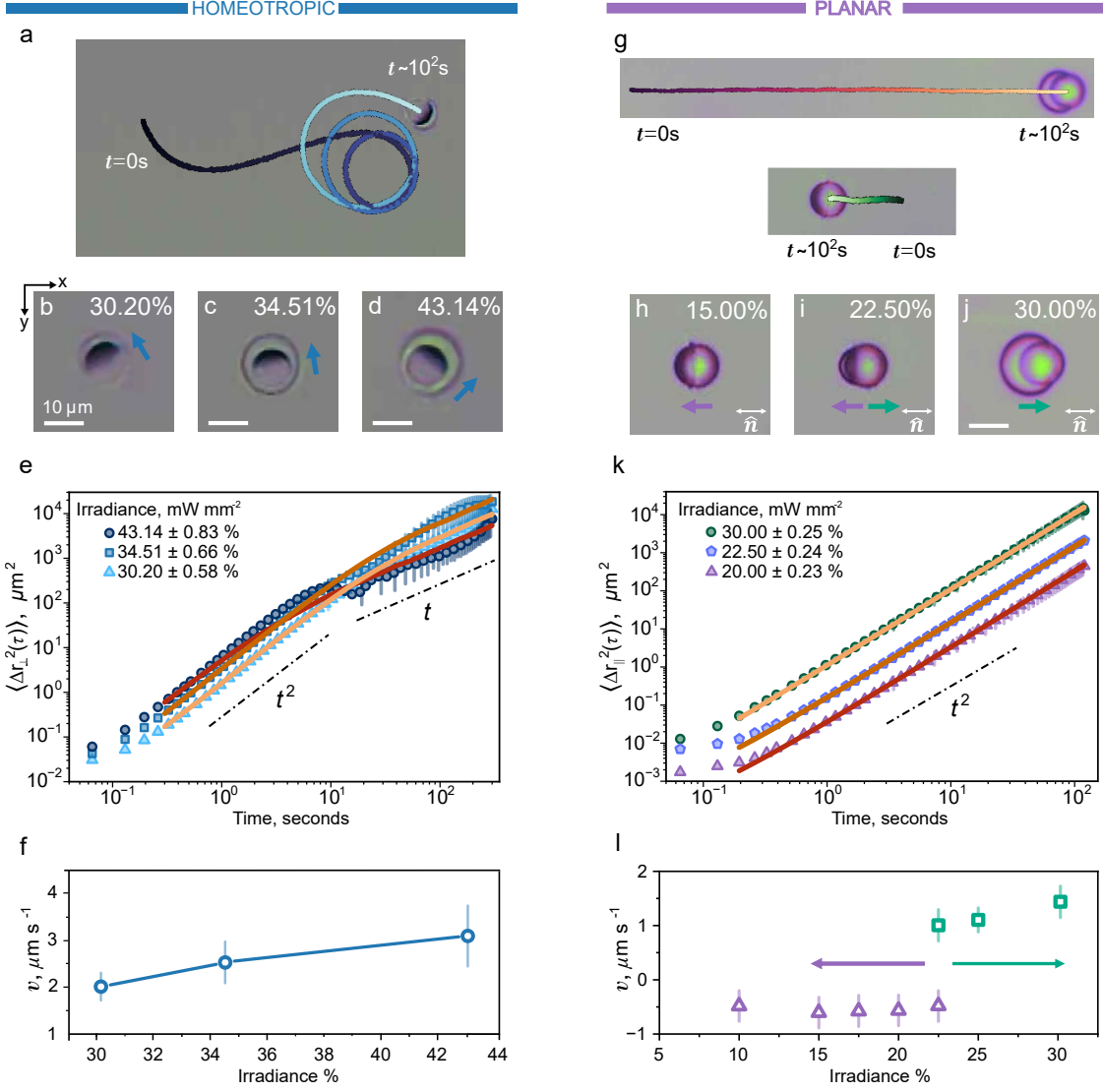


Figure 3: Trajectory analysis of the light-activated Janus colloids for homeotropic (left) and planar (right) confinements. **a,g** Trajectories of representative active colloids. Lighter path colors indicate longer times. **b, c, d, h, i, j** Bright-field optical microscopy images for different irradiances with arrows indicating the direction of the self-propulsion. Note that the area covered by the isotropic phase increases with irradiance. **e,k** Experimental mean-squared displacement of the colloids for different irradiances. Continuous lines represent the MSD of our theoretical models (3) and (4) with the parameters given in Table 1. All irradiance values are given in units of mW mm^{-2} . **f,l** Self-propulsion speed as a function of the light intensity percentages. For planar anchoring, negative (positive) values indicate a speed directed toward (away) the coated side.

For planar confinement, the self-propulsion of the colloid is directed along the nematic director, which we assume to be in the x direction. In addition, the

particle is also subject to surrounding thermal fluctuations, so that we model its dynamics as

$$\dot{\mathbf{r}} = v e_x + \sqrt{2T}\boldsymbol{\eta}, \quad (4)$$

where T controls the magnitude of the fluctuations, v is the self-propulsion speed, and $\boldsymbol{\eta}$ is a Gaussian vector with independent components of unit variance. The MSD of dynamics (4) features two distinct regimes; a diffusive one at short times where $\langle \Delta \mathbf{r}^2 \rangle \sim 4Tt$ and a ballistic one at long times where $\langle \Delta \mathbf{r}^2 \rangle \sim v^2 t^2$. Using our experimental determination of the MSD, we extract the values of T and v . The corresponding results are reported in Table 1 in the Methods. Finally, we simulated (4) and superimposed the MSD on top of its experimental counterpart in Fig. 3k.

Quorum sensing

We now discuss the many-body dynamics of the light-activated Janus colloids. As shown in Fig. 4, the collision of two particles provokes the merging of their isotropic bubbles. At the end of this collision, the two Janus colloids form a cluster entirely surrounded by a larger isotropic bubble (see Fig. 4a and e). As shown in Fig. 4b and f, surrounding single Janus colloids can further aggregate to this two-particle cluster through additional collisions. At the end of this aggregation process, the isotropic bubble ends up encompassing all the colloids once again: it *swallows* the newly aggregated particle. As the cluster aggregates more and more colloids, its surrounding isotropic bubble becomes increasingly more spherical. This loss in asymmetry results in a corresponding decrease in the motility of the cluster with its size, as observed in the plots of Fig. 4c and g. This many-body clustering scenario is qualitatively independent of the confinement type, be it homeotropic (see Mov5) or planar (see Mov6). We thus report only quantitative differences between these two cases, such as the actual speed of dimers, trimers, and larger clusters.

We effectively model the many-body interactions by iterating two operations at each time step of the dynamics. First, we construct the graph \mathcal{G} whose nodes correspond to the positions of the particles and whose edges connect the particles i and j only if their distance satisfies $|\mathbf{r}_i - \mathbf{r}_j| < 1$. Second, we attribute a quorum-sensing, density-dependent motility $v(\rho)$ to each connected component \mathcal{C} of the graph \mathcal{G} . The latter is routinely done in the active matter community, where a sufficiently decreasing density-dependent motility is known to trigger Motility-Induced Phase Separation (MIPS). In addition, inside each connected cluster \mathcal{C} , we model the dynamics of the particles with pairwise Hookean interactions. This prevents particles from leaving the cluster, while leaving the dynamics of

its center of mass unaffected. Following our measurements performed in Fig. 4, we assume that the speed of the clusters $v(\rho)$ is an exponentially decreasing function,

$$v(\rho_{\mathcal{C}}) = v \exp(-\lambda(\rho_{\mathcal{C}} - 1)), \quad (5)$$

where $\rho_{\mathcal{C}}$ is the total number of particles present in the cluster \mathcal{C} . In (5), v is the speed of a single activated colloid and λ characterizes the decay of the cluster's speed with its density. Although we already extracted the experimental value of v (see Table 1), we still need to evaluate λ . To this aim, we fit the experimental values of the cluster's speeds (Fig. 4c and g) to an exponential decay with the density. The resulting values of λ for the two confinement scenarios are reported in the caption of Fig. 4. We now couple the quorum-sensing interactions (5) to the single-body models developed in Section 18 to arrive at many-body descriptions for both planar and homeotropic confinements.

With homeotropic confinement, we assume that the center of mass $\mathbf{r}_{\mathcal{C}}$ of cluster \mathcal{C} evolves according to

$$\dot{\mathbf{r}}_{\mathcal{C}} = v(\rho_{\mathcal{C}})\mathbf{u}(\phi_{\mathcal{C}}) + \sqrt{2T}\boldsymbol{\eta}_{\mathcal{C}}, \quad \dot{\phi}_{\mathcal{C}} = \sqrt{2D}\xi_{\mathcal{C}}, \quad (6)$$

where $v(\rho_{\mathcal{C}})$ is given by (5) while $\boldsymbol{\eta}_{\mathcal{C}}$'s and $\xi_{\mathcal{C}}$ are Gaussian white noises such that $\langle \eta_{\mathcal{C}}^{\alpha}(s)\eta_{\mathcal{C}'}^{\beta}(t) \rangle = \delta_{\alpha\beta}\delta_{\mathcal{C}\mathcal{C}'}\delta(t-s)$ and $\langle \xi_{\mathcal{C}}(s)\xi_{\mathcal{C}'}(t) \rangle = \delta_{\mathcal{C}\mathcal{C}'}\delta(t-s)$.

With planar confinement, the clusters are restricted to self-propel in the e_x direction. We therefore model the evolution of the center of mass $\mathbf{r}_{\mathcal{C}}$ according to

$$\dot{\mathbf{r}}_{\mathcal{C}} = v(\rho_{\mathcal{C}})e_x + \sqrt{2T}\boldsymbol{\eta}_{\mathcal{C}}, \quad (7)$$

where $\boldsymbol{\eta}_{\mathcal{C}}$ is a noise similar to that in (6).

Using our experimental estimates for λ , v , T and D (see Table 1), we performed numerical simulations of (6) and (7). For both confinements, we found that the many-body dynamics leads to a clustering phenomenon similar to the one observed in the experimental setting, thereby confirming the plausibility of our theoretical descriptions (see the time evolution simulation snapshots in Fig. 4d and h, as well as the supplementary movies Mov7 and Mov8).

The clustering mechanism at play in our experiments and simulations is distinct from Motility-Induced Phase Separation since particles, once aggregated to a cluster, are precluded from leaving it: a feature not present in MIPS models. This difference entails noticeable deviations from MIPS’ phenomenology, one of them being that the phase separation we observe does not completely coarsen into a single dense cluster coexisting with a dilute background.

Outlook

We have introduced a versatile experimental platform in which, upon illumination, Janus particles can be induced to self-propel in a nematic liquid crystal. We demonstrated that this new self-propulsion mechanism has two important consequences. First, it allows for an external control of the colloids’ self-propulsion by adjusting the mesogens’ anchoring at the surface of the platform. Second, it mechanically endows the particles with quorum-sensing interactions, producing a local slowing down of motility with the local density. Our experimental platform paves the way toward a finer control of active assemblies endowed with life-like properties.

Acknowledgements

A. T.-V. thanks Prof. Erick Sarmiento-Gómez for the discussions and technical feedback on the experiments and data analysis, Prof. Teresa Lopez-Leon for fruitful discussions, Dr. Zhengyang Liu and Lars Kürten for the suggestions on the particle tracking methodology, and M.Des. Deydreh Martinez-Alvarez for the technical support of the figures. The authors gratefully acknowledge Prof. Stuart Rowan for sharing their polarized optical microscope, which allowed us to perform the experiments. This work used the Searle Cleanroom at the University of Chicago, funded by award number C06RR028629 from the National Institutes of Health - National Center for Research Resources. Instrumentation was purchased with generous funding provided by The Searle Funds at The Chicago Community Trust (Grant A2010-03222). This work was also supported by the University of Chicago Materials Research Science and Engineering Center, which is funded by the National Science Foundation under award number DMR-2011854.

Methods

Experimental setup. Our Janus particles are 10 μm silica spheres prepared according to standard protocols [24], and half-coated with a 30 nm titanium layer. Their motility was constrained to 2D using 12 μm spacers between the upper and lower glass cell walls. To induce homeotropic or planar anchoring of the liquid crystal, we treated the surfaces with DMOAP or brushed them with a microfiber fabric after a polyvinyl alcohol (PVA) spin-coating. The temperature of the confined LC was globally maintained at $35.40 \pm 0.01^\circ\text{C}$, in the nematic phase, by a dual top-bottom heating stage. To activate the colloids, we used a LED source of nominal output power 500 mW with a narrow spectrum line peaked at $\lambda = 542 \text{ nm}$. We recorded particle trajectories at 15 fps with a spatial resolution of 0.14006 $\mu\text{m}/\text{pixel}$ at best. Therefore, the minimum measurable MSD accuracy is of the order of $\sim 10^{-2} \mu\text{m}^2$ and the minimum measurable lag-time is $\sim 0.065 \text{ s}$. Detailed information on every apparatus used and on the fabrication protocol can be found in the Appendix A.

Experimental measurements. For tracking the Janus particles’ center of mass, we followed standard protocols [25, 26] and used ImageJ Fiji software [27] together with Trackpy [28] for movie processing. The MSD is then computed as $\langle \Delta r^2(\tau) \rangle := \frac{1}{n} \sum_{i=1}^n \Delta r_i^2(\tau)$ where $\Delta r_i^2(\tau) := [r(t_i + \tau) - r(t_i)]^2$, $n = N - \tau/\Delta t$, with N the total number of measurements, Δt the sampling frequency, τ the lag time and $t_i = i\Delta t$ ($i \in 0..N$).

Numerical simulations. Our approach to modeling the LC surrounding the particle relies on a non-equilibrium, boundary-driven energy minimization. We focused on simulating the nematic phase of the LC and modeled the isotropic bubble as a fixed surface with planar anchoring, which is a good approximation of the experimental observations. We assume the LC’s total free energy \mathcal{F}_{tot} to be given by

$$\mathcal{F}_{tot} = \int_V [f_{LdG}(\mathbf{Q}) + f_{FR}(\mathbf{Q})] dV + \int_{\partial V} f_s(\mathbf{Q}) d\mathbf{S}, \quad (8)$$

where \mathbf{Q} is the nematic traceless tensor, f_{LdG} is the Landau-de Gennes energy, f_{FR} the Franck–Riesler elastic energy and f_s the surface anchoring energy ensuring the right boundary conditions for \mathbf{Q} . To

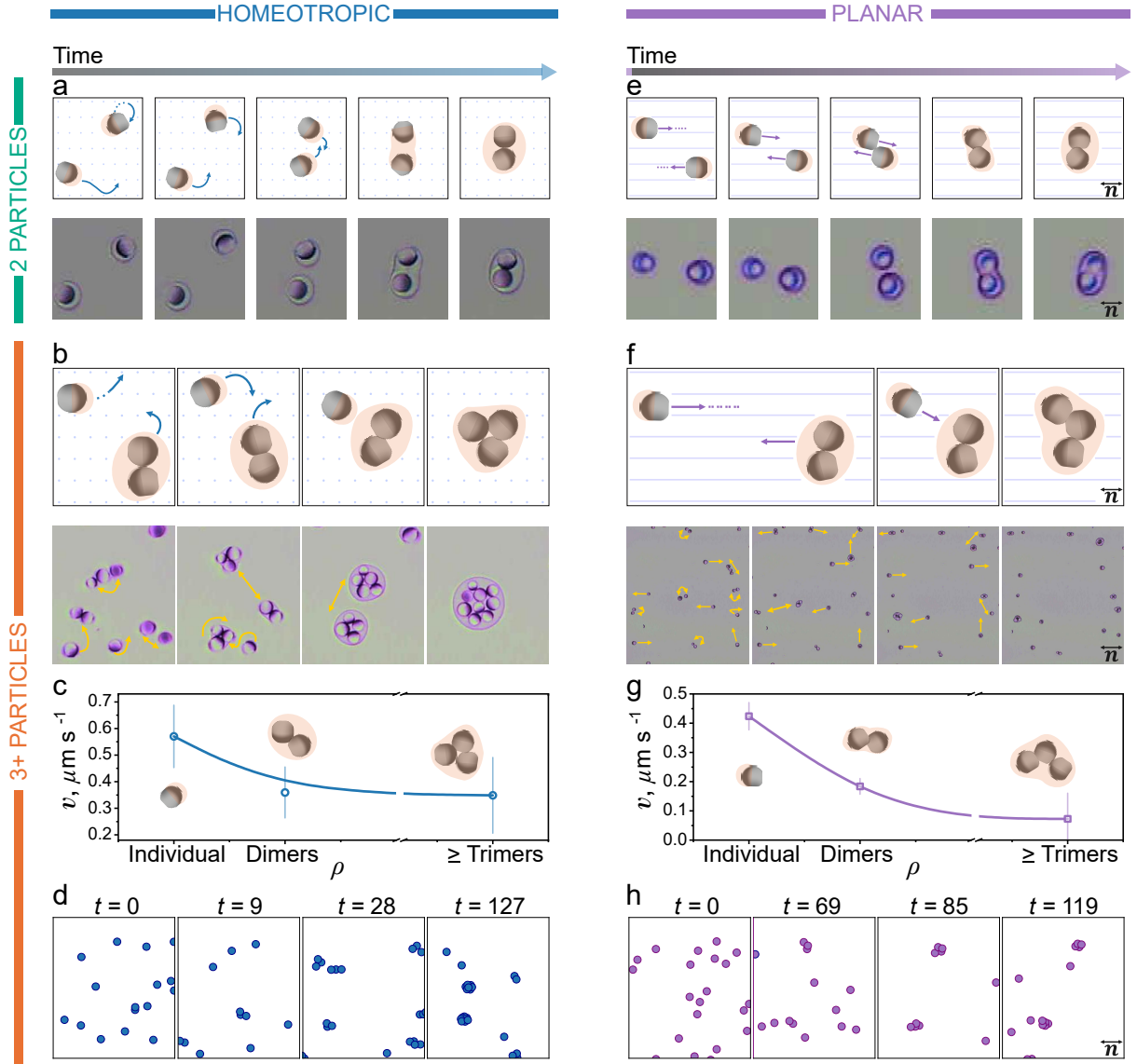


Figure 4: Many-body dynamics of the active colloids for homeotropic (left) and planar (right) confinements, starting with the two-body dynamics (first row) before the three-body dynamics (second row). **a, e** Schematic of the two-body evolution (top subrow) with their corresponding experimental snapshots (bottom subrow). **b, f** Schematic of the many-body evolution (top subrow) with their corresponding experimental snapshots (bottom subrow). **c, g** Experimental self-propulsion speed of one-body, two-body and three-or-above-body clusters. Plain lines are fits (performed in log-log) to (5) with $\lambda = 0.24$ (c) and $\lambda = 0.88$ (g). **d, h** Numerical simulations of quorum-sensing active dynamics (6) with $D = 0.096, T = 0.02, v = 1.25, \lambda = 0.24$ (d) and $D = 0, T = 0.01, v = 1.0, \lambda = 0.88$ (h). The time numbers indicate the time step for each snapshot.

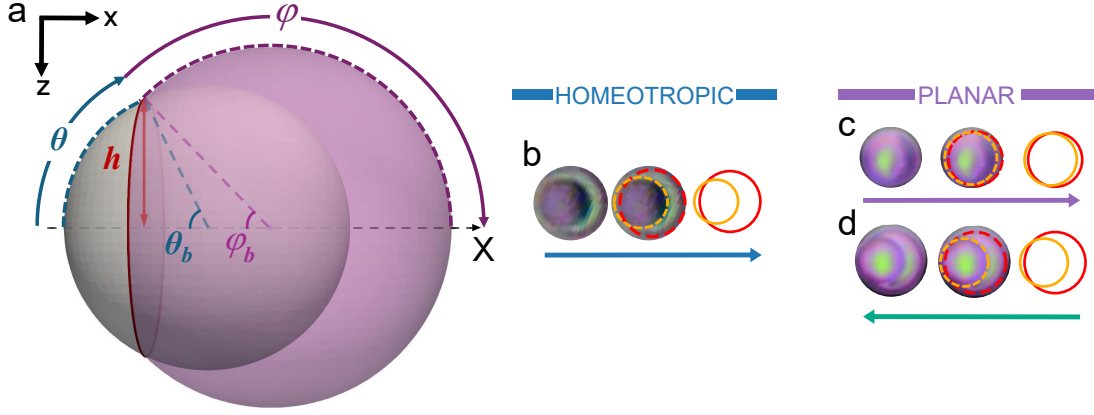


Figure 5: Geometrical configuration extracted from experimental observations. **a** Schematic showing the definitions of θ , φ , θ_b , φ_b , and h . **b,c,d** Determination of the isotropic bubble and its relative position with respect to the particle center from experimental images for both homeotropic (**b**) and planar confinement (**c, d**).

model light activation, we assume that \mathcal{F}_{tot} is further coupled to a spatially varying temperature T , which disrupts the orientation of the mesogens. As f_{LdG} controls the nematic-isotropic transition through the parameter U , a natural way to enforce the coupling to temperature is to consider a T -dependent U (see details in Appendix B). In the bulk, considering an isotropic homogeneous thermal conductivity, the steady-state temperature and nematic tensor are given by

$$\nabla^2 T = 0, \quad \frac{\delta f_{LdG}}{\delta \mathbf{Q}} + \frac{\delta f_{FR}}{\delta \mathbf{Q}} = 0. \quad (9)$$

We further need to specify the boundary conditions for T and \mathbf{Q} ; at the contact surface with the isotropic bubble, they obey

$$T = T_h, \quad \mathbf{n} \cdot \frac{\partial f_{FR}}{\partial \nabla \mathbf{Q}} - \frac{\partial f_s}{\partial \mathbf{Q}} = 0, \quad (10)$$

where T_h is a fixed warm temperature, \mathbf{n} is the normal unit vector on the surface and f_s ensures planar anchoring. Likewise, at the boundary with the Janus particle, the fields respect

$$T = T_c, \quad \mathbf{n} \cdot \frac{\partial f_{FR}}{\partial \nabla \mathbf{Q}} - \frac{\partial f_s}{\partial \mathbf{Q}} = 0, \quad (11)$$

where T_c is a fixed cold ambient temperature and f_s ensures homeotropic anchoring (see details in Appendix B). Finally, we enforced periodic boundaries in the x and y directions while distinguishing the two different scenarios for the cell boundaries in

the z direction: (i) planar and (ii) homeotropic anchoring. After finding \mathbf{Q} and T , the force \mathbf{F} exerted on each surface point of the compound particle–bubble is obtained as [29, 30]

$$F_j = \left(-\frac{\partial f_{FR}}{\partial (\partial_k Q_{pq})} \partial_j Q_{pq} + (f_{FR} + f_{LdG}) \delta_{jk} \right) \nu_k, \quad (12)$$

where summation over repeated indices is implied. ν_k is the k -th unitary vector normal to the particle-bubble surface. Summing this formula over the surface of the compound then yields the total self-propulsion force F_x . Note that in our simulations we approximated the bubble's surface to be a spherical hull whose radius we retrieved in experimental pictures of the compound (see Fig. 5b-d).

Self-propulsion force. Due to rotational symmetry around the x axis, the pressure component of the self-propulsion force is directed along e_x . Its amplitude F_x^P is given by

$$F_x^P = \int_{S_p} P_p d\mathbf{S} + \int_{S_b} P_b d\mathbf{S}, \quad (13)$$

where S_p is the bare surface of the particle and S_b represents the isotropic bubble surface. To simplify the derivation of F_x^P , we introduce in Fig. 5 two spherical coordinate systems with distinct origins; one is centered on the particle while the other is centered on the isotropic bubble such that $S_p = \{(R_p, \theta, \psi), (\theta, \psi) \in [0, \pi] \times [0, 2\pi]\}$ in the former and $S_b = \{(R_b, \varphi, \psi), (\varphi, \psi) \in [0, \pi] \times [0, 2\pi]\}$ in

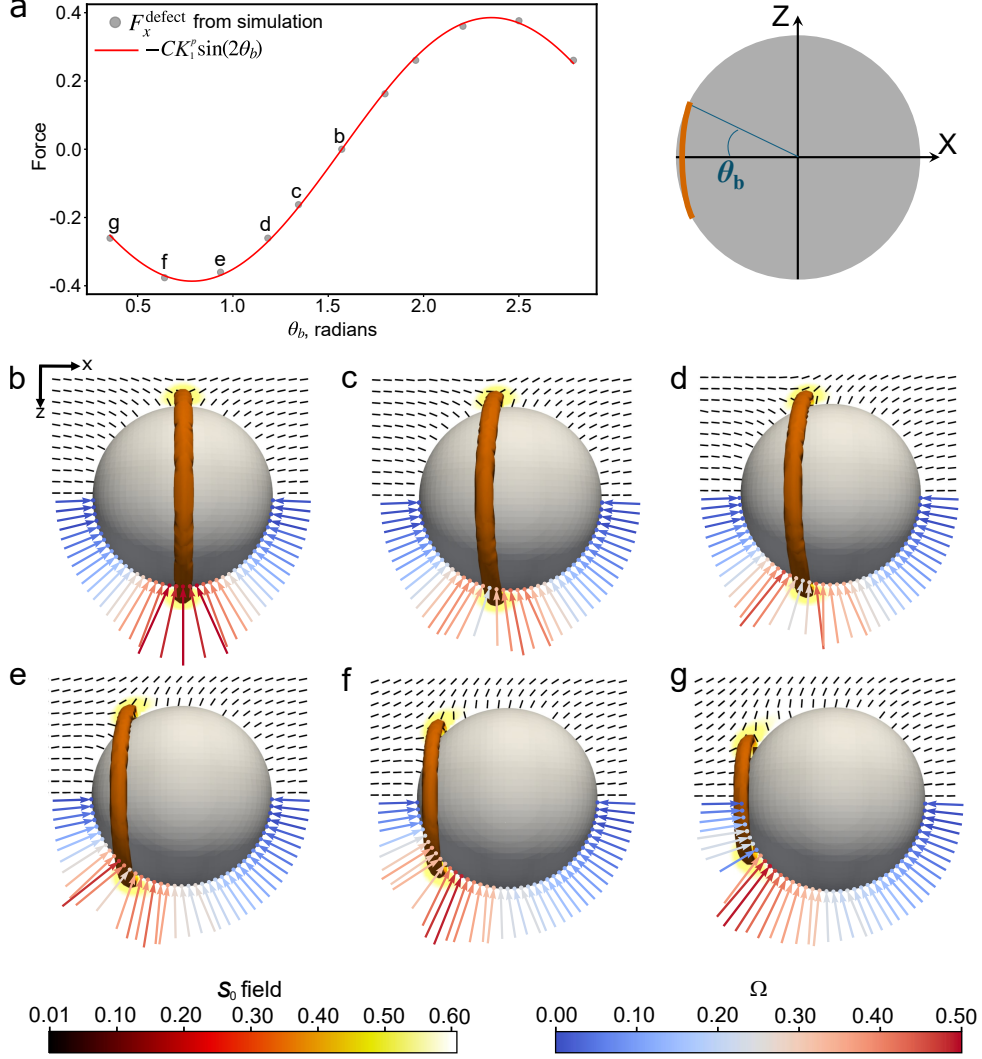


Figure 6: Force distribution on a passive particle with planar confinement. **a** F_x^{defect} as a function of the Saturn ring's position θ_b . Dots indicate numerical results while the plain line corresponds to theoretical prediction (18). **b–g** Numerical force distributions on the particle's surface for $\theta_b = \pi/2, 1.344, 1.183, 0.935, 0.641,$ and $0.355,$ respectively. The scalar nematic order parameter S_0 allows the visualization of the defects while the arrow colormap Ω indicates the magnitude of the force's component due to the presence of defects, namely $\sigma^{\text{defect}} dS$. It is defined as $\Omega = \left| \frac{\mathbf{F}_{sim} \cdot \mathbf{P}_p}{|\mathbf{F}_{sim}|^2} - 1 \right|$, with \mathbf{F}_{sim} the numerically computed force and \mathbf{P}_p the pressure on the particle surface. Thus, Ω deviates from zero only when the local defects contribute to the force.

the latter. We further define θ_b and φ_b as the polar angles of the contact line between the particle and the bubble in both polar coordinate systems, respectively (see Fig. 5a). Using these definitions, we obtain the

following:

$$F_x^P = \int_0^{\theta_b} \pi P_p R_p^2 \sin 2\theta d\theta + \int_{\varphi_b}^{\pi} \pi P_b R_b^2 \sin 2\varphi d\varphi, \quad (14)$$

which can be further simplified into

$$F_x^P = \pi h^2 (P_p - P_b), \quad (15)$$

where $R_p \sin \theta_b = R_b \sin \varphi_b = h$ is the radius of the contact line between the bubble and the particle.

We now determine the additional force exerted by the LC topological defects on the particle in the case of planar confinement. In the absence of light, the defect ring of the particle is located in the yz plane corresponding to $\theta = \pi/2$ and does not generate any net self-propulsion force. However, if this ring is displaced away from $\theta_b = \pi/2$, we intuitively expect the emergence of a net force that tends to push back the particle in the rest configuration corresponding to $\theta_b = \pi/2$. In addition, $\theta_b = 0$ or π correspond to hedgehog defects: These are stable configurations for which we expect $F_x^{\text{defect}} = 0$. The most simple π periodic function that is odd with respect to $\pi/2$ and then vanishes at $\theta_b = 0 \bmod \pi$ is $\sin(2\theta_b)$. We therefore infer (18), where C is a constant. Our intuitive expression (18) agrees nearly perfectly with the result of our simulations (see Fig. 6). Additional simulation details are provided in Appendix B.

Fitting parameters. To fit T , v and D , we proceed in three steps for each intensity of light. Using $\langle \Delta \mathbf{r}^2(t) \rangle$ as a function of time on the logarithmic scale, we isolate the time range where it exhibits ballistic behavior. Fitting this time range to $v^2 t^2$ allows us to retrieve the particle's speed v . Focusing on smaller time scales, we then fit the mean square displacement to $4Tt + v^2 t^2$, hence obtaining the translational diffusion T . Finally, on the largest time scales, we fit the MSD to $(4T + 2v^2/D)t$, thereby retrieving the angular diffusion D . The resulting fitted parameters are shown in Table 1.

Irradiance mW mm^{-2}	v	T	D
<i>homeotropic confinement</i>			
$30.20 \pm 0.58 \%$	1.20	0.019	0.096
$34.51 \pm 0.66 \%$	1.84	0.026	0.095
$43.14 \pm 0.83 \%$	2.45	0.067	0.705
<i>planar confinement</i>			
$20.00 \pm 0.23 \%$	0.17	0.0014	-
$22.50 \pm 0.24 \%$	0.69	0.0026	-
$30.00 \pm 0.25 \%$	1.03	0.010	-

Table 1: Values of v , T and D fitted from the experimental MSD. Note that we set $D = 0$ for planar confinement according to (4).

Appendix A Experimental methods

Sample preparation. Janus particles were prepared by standard methods [24] using 10 μm silica spheres functionalized with amine groups (CD Bioparticles, NY USA). A 30 nm layer of titanium was deposited on top of the particles (AJA ATC-Orion 8E e-beam evaporation system, AJA International Inc, MA USA), verified by electron microscopy (FEI Quanta 650 FEG SEM, Thermo Fisher Scientific Inc, USA). Afterward, to induce LC surface homeotropic anchoring on the Janus particles, they are suspended in a 2% deionized water solution (18.2 M Ω cm, Millipore, Bedford, MA USA) of dimethyloctadecyl[3-(trimethoxysilyl)propyl]ammonium chloride (DMOAP) (Sigma-Aldrich, USA) for 15 min, then rinsed profusely with deionized water, and finally baked at 100°C for one hour. The dried Janus particles are mixed at a dilute concentration of 0.01 wt% in 4-Cyano-4'-pentylbiphenyl (5CB) LC, purchased from Hebei Maison Chemical Co., Ltd (China). Thermogravimetric measurements were performed with a TGA instrument (TA Instruments, USA) to ensure the final particle concentration. We built cells to confine the LC-particle suspension for experimental observations using soda-lime glass microscope slides (Thermo Scientific, NH USA). To induce homeotropic anchoring on the glass cell, we cleaned the glass slides with a half-half mixture of ethanol and acetone, then rinsed with deionized water and air plasma treatment to eliminate any trace of organic pollutants. Later, the glass slides were also treated with DMOAP. To induce planar anchoring, we cleaned the glass slides with piranha solution (70% H₂SO₄ (95.0%-98.0% pure, Sigma-Aldrich, USA), 30% H₂O₂ (30% dilution, Fisher Scientific, PA USA)) and then rinsed profusely with deionized water. The glass slides were then dried with nitrogen. Subsequently, we spin-coated each slide for 90 s with an aqueous solution of polyvinyl alcohol (PVA) at 10 wt% and a molecular weight of 13 kDa (Sigma-Aldrich, USA). After spin coating, the slides were baked for one hour at 100°C. Then, we brushed each coated slide in one direction with a clean velvet fabric to create micro-grooves. The adhesiveness of the polymer alongside the microgrooves that are etched onto the polymer yields the planar anchoring of the LC mesogens. After brushing, we oriented the top and bottom glass pieces of the cell so that their brushing was in opposite directions to ensure homogeneity. For both homeotropic and planar anchoring cases, we used 12 μm thick mylar films as cell spacers (Premier Lab Supply, FL USA), and 5-minute epoxy resin to seal cells (Devcon, MA USA). Slight variations in the cell thickness are possible due to the method of assembly. The LC colloidal suspension was then heated to 50°C and gently introduced into the glass cells by capillary effects. Cells were immediately sealed with 5-minute epoxy resin and removed from the hot plate to quench the system; otherwise, Janus particles would reorganize and cluster because they are prone to being dragged by the nematic-isotropic (NI) interface. The LC was allowed to relax to obtain perfect homeotropic or parallel alignment.

Light activation and microscopy. We use the AURA III LED engine (Lumencor, OR USA) as the activation source (bandpass filter $\lambda = 542$ nm, FWHM = 33 nm. Maximum nominal output power = 500 mW). Light-power measurements are performed using a Thorlabs PM160T power meter (USA). The light source is assembled into a Leica DM-2700P polarizing microscope (Germany) in reflection mode using a liquid light guide and a collimator. We use a custom-made filter cube (Chroma Technologies, USA; dichroic mirror % $T \geq 95\%$ for $470 \text{ nm} \leq \lambda \leq 480 \text{ nm}$, % $R \geq 95\%$ for $495 \text{ nm} \leq \lambda \leq 545 \text{ nm}$, and transmission filter % $T \geq 95\%$ for $445 \text{ nm} \leq \lambda \leq 470 \text{ nm}$ and $605 \text{ nm} \leq \lambda \leq 650 \text{ nm}$). The collimated light beam passes through an N-Plan achromatic objective of 20 \times magnification (for the homeotropic anchoring experiments) or and objective of 50 \times magnification (for the planar anchoring experiments). Simultaneously, a white LED source is used in transmission mode to image the sample. Movies are recorded with a Leica MC170 HD camera. Bright-field and polarized movies are recorded at 15.3735 fps, and the camera's spatial resolution is 0.34662 $\mu\text{m}/\text{pixel}$ when using the 20 \times objective, and 0.14006 $\mu\text{m}/\text{pixel}$ when using the 50 \times objective. Therefore, the minimum MSD that can be measured is of the order of $\sim 10^{-2} \mu\text{m}^2$ and the minimum measurable lag-time is ~ 0.065 s.

Temperature control. We use a dual top-bottom heating stage HCS402 and a high-precision temperature controller mk2000 (resolution 0.001°C; INSTEC, USA) to maintain samples at constant $35.40 \pm 0.01^\circ\text{C}$ in the nematic phase.

Particle tracking analysis. ImageJ Fiji distribution software [27] was used for movie processing. For proper

tracking of the center of mass of Janus particles in the case of cells with homeotropic anchoring, standard protocols were followed and can be found elsewhere [25, 26]. Once the coordinates of the center of mass of the particles were computed, the trajectory paths were displayed using Trackpy [28]. For the planar anchoring case, the particle's tracking analysis was performed using the ImageJ TrackMate plugin [31].

Mean-squared displacement computation. To obtain the MSD from the trajectories of Janus particles, the γ -position of the particle as a function of time, $r_{b,\gamma}(t)$, is tracked. Where $t = i\Delta t$, $1/\Delta t$ is the sampling frequency of the particle tracking technique, N is the total number of measurements and $i = 0, 1, 2, 3, \dots, N$. The MSD is then computed as, $\langle \Delta r_\gamma^2(\tau) \rangle := \frac{1}{n} \sum_{i=1}^n \Delta r_{i,\gamma}^2(\tau)$ where $\Delta r_{i,\gamma}^2(\tau) := [r_{b,\gamma}(t + \tau) - r_{b,\gamma}(t)]^2$, $n = N - \tau/\Delta t$, τ is the lag-time and the sub-index γ indicates the spatial direction of the measurement, γ can be either parallel, \parallel , or perpendicular, \perp , to the nematic director, $\hat{\mathbf{n}}$. Experiments with a homeotropic anchoring at the walls of the glass cell allow measuring $\langle \Delta r_\perp^2(\tau) \rangle$ while experiments with planar anchoring at the walls of the glass cell allow measuring $\langle \Delta r_\parallel^2(\tau) \rangle$.

Appendix B Numerical implementation

A nematic LC can be described by a tensorial order parameter \mathbf{Q} . For a uniaxial nematic LC, $\mathbf{Q} = S_0(\mathbf{nn} - \mathbf{I}/3)$, where the unit vector \mathbf{n} represents the nematic director field, S is the scalar order parameter of the nematic LC, and \mathbf{I} is the identity tensor. The total free energy of a nematic LC comprises the Landau–de Gennes short-range free energy density f^{LdG} , the long-range elastic energy density f^{el} , and the anchoring-induced surface free energy density f^{surf}

$$\mathcal{F}_{\text{total}} = \int_V (f^{\text{LdG}} + f^{\text{el}}) dV + \int_{\partial V} f^{\text{surf}} dS, \quad (\text{B1})$$

where V and ∂V are the volume and surface of the region of interest. The Landau–de Gennes free energy f^{LdG} is given by

$$\begin{aligned} f^{\text{LdG}} = & \frac{A_0}{2} \left(1 - \frac{U}{3} \right) \text{Tr}(\mathbf{Q}^2) - \frac{A_0 U}{3} \text{Tr}(\mathbf{Q}^3) \\ & + \frac{A_0 U}{4} (\text{Tr}(\mathbf{Q}^2))^2, \end{aligned} \quad (\text{B2})$$

where the parameter A_0 is the energy density scale and U controls the equilibrium magnitude of S_0 through

$$S_0 = \frac{1}{4} + \frac{3}{4} \sqrt{1 - \frac{8}{3U}}. \quad (\text{B3})$$

The elastic free energy f^{el} can be expressed using the Einstein summation notation as

$$\begin{aligned} f^{\text{el}} = & \frac{1}{2} L_1 (\partial_k Q_{ij}) (\partial_k Q_{ij}) + \frac{1}{2} L_2 (\partial_k Q_{jk}) (\partial_l Q_{jl}) \\ & + \frac{1}{2} L_3 Q_{ij} (\partial_i Q_{kl}) (\partial_j Q_{kl}) + \frac{1}{2} L_4 (\partial_l Q_{jk}) (\partial_k Q_{jl}). \end{aligned} \quad (\text{B4})$$

Here, the coefficients L_1 , L_2 , L_3 , and L_4 can be mapped to the Frank elastic constant K_1 , K_2 , K_3 , and K_{24} , which are the splay, twist, bend, and saddle-splay modulus, respectively, through

$$\begin{aligned} L_1 &= \frac{1}{2S_0^2} \left[K_2 + \frac{1}{3} (K_3 - K_1) \right], \\ L_2 &= \frac{1}{S_0^2} (K_1 - K_{24}), \\ L_3 &= \frac{1}{2S_0^3} (K_3 - K_1), \\ L_4 &= \frac{1}{S_0^2} (K_{24} - K_2). \end{aligned} \tag{B5}$$

In our simulations, we set $L_1 = 1$ and $L_2 = L_3 = L_4 = 0$, equivalent to $K_1 = K_2 = K_3 = K_{24} = 0.758$, and $A_0 = 1$. The surface anchoring free energy f^{surf} is given by

$$f^{\text{surf}} = \frac{1}{2} W (\mathbf{Q} - \mathbf{Q}_{\text{surf}})^2. \tag{B6}$$

Here, \mathbf{Q}_{surf} is the preferred field of the surface, and W is the anchoring strength.

To obtain a stable solution of the nematic LC, we minimize the total free energy. We define a molecular field as

$$\mathbf{H} = - \left[\frac{\delta \mathcal{F}_{\text{total}}}{\delta \mathbf{Q}} \right]^{st}, \tag{B7}$$

where $[\dots]^{st}$ is a symmetric and traceless operator. Assuming that all transitions are quasistatic processes, the evolution of the \mathbf{Q} -tensor for bulk points follows

$$\partial_t \mathbf{Q} = \Gamma_s \mathbf{H}, \tag{B8}$$

where $\Gamma_s = \Gamma/\xi_n$ is the relaxation constant. Here, Γ is related to the rotational viscosity γ_1 of LC by $\Gamma = 2S_0^2/\gamma_1$ and ξ_n is the nematic coherence length. For surface points, the evolution of the \mathbf{Q} -tensor is governed by

$$\frac{\partial \mathbf{Q}}{\partial t} = -\Gamma_s \left[\boldsymbol{\nu} \cdot \frac{\partial \mathcal{F}}{\partial \nabla \mathbf{Q}} + \left\{ \frac{\partial f^{\text{surf}}}{\partial \mathbf{Q}} \right\}^{st} \right], \tag{B9}$$

where the unit vector $\boldsymbol{\nu}$ represents the surface normal (pointing outside of the LC domain).

In the simulation, we define the bubble and particle regions according to the experimental images. On the bubble surface, a degenerate planar anchoring condition is assumed. A homeotropic anchoring condition is imposed on the surface of the particle with $W = 1$. Because the LC is in the isotropic phase inside the bubble region (denoted as Ω), we therefore only evolve the \mathbf{Q} -tensor outside the particle and bubble region using the above numerical approach.

We assume that the parameter U in (B2) is linearly dependent on the local temperature T according to $U = 3.5 - 0.325 \times T$. The temperature field T satisfies the Poisson equation $\frac{\partial T}{\partial t} = \nabla \cdot (\kappa \cdot \nabla T)$, where κ is the thermal conductance tensor [32]. For simplicity, we only consider an isotropic conductivity tensor $\kappa = \kappa_0 \mathbf{I}$ with $\kappa_0 = 1$ in the simulation. The temperature on the surface of the unheated particle and the boundaries of the solution domain are set at 0, while the temperature on the heated bubble surface is set at $T = T_{\text{cut-off}}$. In our discretized simulation,

we update the temperature field from step n to step $n + 1$ according to

$$\begin{aligned}
T_{i,j,k}^{n+1} &= T_{i,j,k}^n + \Delta t \cdot \left(\frac{T_{i+1,j,k}^n + T_{i-1,j,k}^n + T_{i,j+1,k}^n}{h^2} \right. \\
&\quad \left. + \frac{T_{i,j-1,k}^n + T_{i,j,k+1}^n + T_{i,j,k-1}^n - 6T_{i,j,k}^n}{h^2} \right), \\
T|_{\partial\Omega_{\text{unheated particle}}} &= T|_{\text{boundary}} = 0, \\
T|_{\partial\Omega_{\text{bubble}}} &= T_{\text{cut-off}}.
\end{aligned} \tag{B10}$$

where i , j , and k denote spatial coordinates, and h denotes the unit size of the mesh in the simulation. From (B3), we know that when $U = \frac{8}{3}$, the system transitions to the isotropic phase, corresponding to a transition temperature of $T_{\text{trans}} = 2.564$ in the simulation units. After bubble formation, its interior becomes isotropic, making $T_{\text{cut-off}} \approx T_{\text{trans}}$. We set $T_{\text{cutoff}} = 2$, slightly below T_{trans} .

After obtaining a stable solution for the molecular field, the force \mathbf{F} exerted by the Ericksen stress on each surface point of the particle and bubble can be calculated using the following equations [29, 30]

$$F_j = \left(-\frac{\partial f^{\text{el}}}{\partial Q_{pq,k}} Q_{pq,j} + (f^{\text{el}} + f^{\text{LdG}}) \delta_{jk} \right) \nu_k. \tag{B11}$$

We have provided simulated director fields for representative homeotropic and planar anchoring cases in Fig. 2 **a, b, c** in the main text. The force in each simulation grid is calculated using (B11). To analyze the force distribution, we transform all simulated forces into spherical coordinates, choosing the $-x$ direction (coaxis of the particle and bubble) as the north-pole direction. The X - Z section through the centers of the particle and bubble is defined as the azimuth angle $\phi = 0$.

To obtain representative force distributions, we average over the azimuthal angle ϕ and plot the distribution on the xz plane on which the polar angle dependence of the pressure is given. This gives the force distribution as a function of θ . The schematics in Fig. 2 **d, e, f** are plotted on the basis of these results. We calculate the total force in the x -direction, F_x and report the value in Fig. 2 in the main text.

In addition, we perform simulations to validate the expression for $F_x^{\text{defect}} = -CK_1^p \sin(2\theta_b)$. Starting from a homeotropic anchoring dipole configuration, that is, a bulk hedgehog defect at the left pole of the particle, we observe a spontaneous transition to a Saturn ring defect at the equator ($\theta_b = \pi/2$). Taking six snapshots during this process, we calculate the force distribution (Fig. 6b-g and F_x on the particle. Fitting the data with $C = 0.5095$ and we have $K_1^p = 0.758$, we find an excellent agreement between the simulated F_x^{defect} and the analytical expression (see Fig. 6a).

References

- [1] Adler, J.: Chemotaxis in bacteria. Annual review of biochemistry **44**(1), 341–356 (1975)
- [2] Berg, H.C.: Chemotaxis in bacteria. Annual review of biophysics and bioengineering **4**(00), 119–136 (1975)
- [3] Hautier, Y., Niklaus, P.A., Hector, A.: Competition for light causes plant biodiversity loss after eutrophication. Science **324**(5927), 636–638 (2009)
- [4] Ballerini, M., Cabibbo, N., Candelier, R., Cavagna, A., Cisbani, E., Giardina, I., Lecomte, V., Orlandi, A., Parisi, G., Procaccini, A., *et al.*: Interaction ruling animal collective behavior depends on topological rather than metric distance: Evidence from a field study. Proceedings of the national academy of sciences **105**(4), 1232–1237 (2008)
- [5] Miller, M.B., Bassler, B.L.: Quorum sensing in bacteria. Annual Reviews in Microbiology **55**(1), 165–199 (2001)

- [6] Cates, M.E., Tailleur, J.: Motility-induced phase separation. *Annu. Rev. Condens. Matter Phys.* **6**(1), 219–244 (2015)
- [7] Howse, J.R., Jones, R.A., Ryan, A.J., Gough, T., Vafabakhsh, R., Golestanian, R.: Self-motile colloidal particles: from directed propulsion to random walk. *Physical review letters* **99**(4), 048102 (2007)
- [8] Theurkauff, I., Cottin-Bizonne, C., Palacci, J., Ybert, C., Bocquet, L.: Dynamic clustering in active colloidal suspensions with chemical signaling. *Physical review letters* **108**(26), 268303 (2012)
- [9] Palacci, J., Sacanna, S., Steinberg, A.P., Pine, D.J., Chaikin, P.M.: Living crystals of light-activated colloidal surfers. *Science* **339**(6122), 936–940 (2013)
- [10] Bricard, A., Caussin, J.-B., Desreumaux, N., Dauchot, O., Bartolo, D.: Emergence of macroscopic directed motion in populations of motile colloids. *Nature* **503**(7474), 95–98 (2013)
- [11] Zöttl, A., Stark, H.: Emergent behavior in active colloids. *Journal of Physics: Condensed Matter* **28**(25), 253001 (2016)
- [12] Zhang, J., Luijten, E., Grzybowski, B.A., Granick, S.: Active colloids with collective mobility status and research opportunities. *Chemical Society Reviews* **46**(18), 5551–5569 (2017)
- [13] Lavergne, F.A., Wendehenne, H., Bäuerle, T., Bechinger, C.: Group formation and cohesion of active particles with visual perception-dependent motility. *Science* **364**(6435), 70–74 (2019)
- [14] Fernandez-Rodriguez, M.A., Grillo, F., Alvarez, L., Rathlef, M., Buttinoni, I., Volpe, G., Isa, L.: Feedback-controlled active brownian colloids with space-dependent rotational dynamics. *Nature communications* **11**(1), 4223 (2020)
- [15] Muiños-Landin, S., Fischer, A., Holubec, V., Cichos, F.: Reinforcement learning with artificial microswimmers. *Science Robotics* **6**(52), 9285 (2021)
- [16] Ben Zion, M.Y., Fersula, J., Bredeche, N., Dauchot, O.: Morphological computation and decentralized learning in a swarm of sterically interacting robots. *Science Robotics* **8**(75), 6140 (2023)
- [17] Geyer, D., Martin, D., Tailleur, J., Bartolo, D.: Freezing a flock: Motility-induced phase separation in polar active liquids. *Physical Review X* **9**(3), 031043 (2019)
- [18] Lefranc, T., Dinelli, A., Fernández-Rico, C., Dullens, R., Tailleur, J., Bartolo, D.: Quorum sensing and absorbing phase transitions in colloidal active matter. *arXiv preprint arXiv:2502.13919* (2025)
- [19] Gu, Y., Abbott, N.L.: Observation of saturn-ring defects around solid microspheres in nematic liquid crystals. *Physical Review Letters* **85**(22), 4719 (2000)
- [20] Mermin, N.D.: Boojums all the way through. *Physics Today*, 46 (1981)
- [21] Tasinkevych, M., Silvestre, N., Da Gama, M.T.: Liquid crystal boojum-colloids. *New journal of physics* **14**(7), 073030 (2012)
- [22] Romanczuk, P., Bär, M., Ebeling, W., Lindner, B., Schimansky-Geier, L.: Active brownian particles: From individual to collective stochastic dynamics. *The European Physical Journal Special Topics* **202**, 1–162 (2012)
- [23] Solon, A.P., Cates, M.E., Tailleur, J.: Active brownian particles and run-and-tumble particles: A comparative

- study. *The European Physical Journal Special Topics* **224**(7), 1231–1262 (2015)
- [24] Conradi, M., Zorko, M., Muševič, I.: Janus nematic colloids driven by light. *Optics Express* **18**(2), 500–506 (2010)
- [25] Cui, J., Long, D., Shapturenka, P., Kretzschmar, I., Chen, X., Wang, T.: Janus particle-based microprobes: Determination of object orientation. *Colloids and Surfaces A: Physicochemical and Engineering Aspects* **513**, 452–462 (2017)
- [26] Anthony, S.M., Hong, L., Kim, M., Granick, S.: Single-particle colloid tracking in four dimensions. *Langmuir* **22**, 9812–9815 (2006)
- [27] Schindelin, J., Arganda-Carreras, I., Frise, E., Kaynig, V., Longair, M., Pietzsch, T., Preibisch, S., Rueden, C., Saalfeld, S., Schmid, B., Tinevez, J.-Y., White, D.J., Hartenstein, V., Eliceiri, K., Tomancak, P., Cardona, A.: Fiji: an open-source platform for biological-image analysis. *Nature Methods* **9**, 676–682 (2012)
- [28] Allan, D.B., Caswell, T., Keim, N.C., Wel, C.M., Verweij, R.W.: Soft-matter/trackpy: V0.6.1 (v0.6.1). Zenodo. <https://doi.org/10.5281/zenodo.7670439>
- [29] Qian, T., Sheng, P.: Generalized hydrodynamic equations for nematic liquid crystals. *Phys. Rev. E* **58**, 7475–7485 (1998) <https://doi.org/10.1103/PhysRevE.58.7475>
- [30] Mou, Z., Zhang, R.: Q-tensor based continuum mechanics of surfaces immersed in nematic liquid crystals. In prep.
- [31] Tinevez, J.-Y., Perry, N., Schindelin, J., Hoopes, G.M., Reynolds, G.D., Laplantine, E., Bednarek, S.Y., Shorte, S.L., Eliceiri, K.W.: Trackmate: An open and extensible platform for single-particle tracking. *Methods* **115**, 80–90 (2017)
- [32] Ahlers, G., Cannell, D.S., Berge, L.I., Sakurai, S.: Thermal conductivity of the nematic liquid crystal 4-n-pentyl-4'-cyanobiphenyl. *Phys. Rev. E* **49**, 545–553 (1994) <https://doi.org/10.1103/PhysRevE.49.545>